

# Superelastic load cycling of Gum Metal

V.A. Vorontsov <sup>a</sup>, N.G. Jones <sup>b</sup>, K.M. Rahman <sup>a</sup>, D. Dye <sup>a</sup>

<sup>a</sup>*Department of Materials, Royal School of Mines, Imperial College, Prince Consort Road, South Kensington, London SW7 2BP, UK*

<sup>b</sup>*Department of Materials Science and Metallurgy, University of Cambridge, 27 Charles Babbage Road, Cambridge, CB3 0FS, UK*

---

## Abstract

The superelastic beta titanium alloy, Gum Metal, has been found to accumulate plastic strain during tensile load cycling in the superelastic regime. This is evident from the positive drift of the macroscopic stress vs. strain hysteresis curve parallel to the strain axis and the change in its geometry subsequent to every load-unload cycle. In addition, there is a progressive reduction in the hysteresis loop width and in the stress at which the superelastic transition occurs. In-situ synchrotron X-ray diffraction has shown that the lattice strain exhibited the same behaviour as that observed in macroscopic measurements and identified further evidence of plastic strain accumulation. The mechanisms responsible for the observed behaviour have been evaluated using transmission electron microscopy, which revealed a range of different defects that formed during load cycling. The formation of these defects is consistent with the classical mathematical theory for the b.c.c. to orthorhombic martensitic transformation. It is the accumulation of these defects over time that alters its superelastic behaviour.

*Key words:* Gum metal; beta titanium alloys; martensitic transformation; synchrotron X-ray scattering; transmission electron microscopy

---

## 1. Introduction

In 2003, Saito et al. [1] presented their findings on a novel metastable  $\beta$ -titanium alloy (Ti-36Nb-2Ta-3Zr-0.3O wt.%), Gum Metal, that exhibited a unique combination of attractive mechanical properties. These included a high tensile strength in excess of 1 GPa, a low elastic modulus of  $\approx 70$  GPa in the hot worked condition ( $\approx 55$  GPa after cold rolling) as well as superelastic and superplastic behaviour. These ‘super’ properties were attained by selecting a composition that simultaneously satisfied three theoretically predicted electronic parameters: electron per atom ratio ( $e/a=4.24$ ), bond order ( $Bo=2.87$ ) and  $d$  electron orbital energy level ( $Md=2.45$  eV).

10 The authors noted that the material exhibited very little hardening even after substan-  
11 tial cold work. Based on this and their microstructural observations, it was stipulated  
12 that the material underwent plastic deformation *via* a dislocation free mechanism. They  
13 claimed that no martensitic transformation took place during cold work. Instead, the  
14 unstable  $\beta$  lattice readily formed giant faults by ideal shear and thus accommodated the  
15 plastic strain. However, the *in-situ* synchrotron X-ray work of Talling et al. [2,3], has  
16 conclusively proven that a reversible stress induced martensitic transformation, whereby  
17 the body-centred cubic (*bcc*)  $\beta$  phase transforms to the orthorhombic  $\alpha''$ , is responsible  
18 for the superelastic behaviour.

19 Despite this, the mechanisms responsible for the peculiar mechanical behaviour of Gum  
20 metal are complex and remain a subject of ongoing work. Morris et al. [4] have shown that  
21 the propensity of Gum Metal for undergoing the martensitic transformation is orientation  
22 and texture dependent. Furthermore, structures commonly referred to as “giant faults”,  
23 nanodisturbances, twinning, dislocations and  $\alpha''$  are typically observed in the  $\beta$  phase  
24 after cold working of Gum Metal as well as other superelastic alloys like Ti-2448 and  
25 Ti-12Mo. Their exact role in the deformation processes remains to be determined, while  
26 there has been no evidence to date that their origin is assisted by dislocation glide [1,5].  
27 Furthermore, cold work results in the formation of large number of fine stress-induced  
28  $\omega$  phase precipitates [6–8]. These have a hexagonal crystal structure that results from  
29 the systematic collapse of the  $\{111\}$  planes in the  $\beta$  phase. Since cold working increases  
30 the tensile strength of Gum Metal, it is likely that the formation of the  $\omega$  phase plays  
31 an important role. Lastly, plasticity that is mediated by dislocation glide has also been  
32 reported in derivative alloys [9,10,5].

33 Due to its low elastic modulus and the low toxicity of niobium as a  $\beta$  stabilising element  
34 [11], Gum Metal is receiving significant attention from the biomedical community as  
35 a candidate material for orthopaedic implants. In addition, the low modulus and the  
36 possibility of hysteretic superelastic behaviour make the alloy interesting to engineers  
37 for energy absorbing applications. Therefore, it is important to understand fully the  
38 mechanical behaviour of Gum Metal during superelastic load cycling.

39 In this work we examine the superelastic behaviour of Gum Metal under cyclic tensile  
40 loading using synchrotron X-ray diffraction and high-resolution electron microscopy. We  
41 show that the  $\beta \rightarrow \alpha''$  martensitic transformation introduces a variety of permanent  
42 lattice defects. This leads to accumulation of plastic strain and changes the shape of  
43 superelastic hysteresis with every load-unload cycle. Finally, we provide an explanation  
44 for this accumulation of defects by employing classical mathematical theory to evaluate  
45 the martensitic transformation in Gum Metal.

## 46 2. Experimental method

### 47 2.1. Material preparation

48 The Gum Metal employed in this study was produced using ingot metallurgy. An  
49 elemental powder compact was melted in a high purity argon atmosphere using a helium  
50 plasma torch. The initial ingot was then triple remelted with inversions. A billet 60 mm  
51 in diameter was machined from the button-shaped ingot. It was then subjected to a 60  
52 minute solution heat treatment at 850 °C. Deltaglaze<sup>TM</sup> 3418 (Acheson, MI, USA) glass

53 lubricant, was subsequently applied to the surface of the billet and it was extruded into  
54 12 mm rod after a 105 minute heat treatment at 975 °C. Inductively coupled plasma  
55 optical emission spectrometry (ICP-OES) was used to verify the chemical composition  
56 of the final product: Ti-36.2Nb-1.96Ta-3.16Zr-0.26O wt.%. (LECO analysers were used  
57 to measure the oxygen and hydrogen content.)

## 58 2.2. *In-situ synchrotron X-ray scattering*

59 The *in-situ* loading experiment was performed at the I12 beamline of the Diamond  
60 Light Source synchrotron X-ray facility in Didcot, Oxfordshire, UK. Figure 1 shows a  
61 schematic representation of the experimental set-up. A ‘dog bone’ tensile test specimen,  
62 with gauge dimensions of 1.5×1.5×19 mm was electric discharge machined (EDM) from  
63 the extruded Gum Metal bar, with the tensile axis aligned parallel to the extrusion  
64 direction. It was subjected to sub-yield cyclic tensile loading between 15 and 700 MPa on  
65 a purpose built 5 kN frame using a loading rate of 4 MPa s<sup>-1</sup>. The maximum stress does  
66 not exceed the yield strength of Gum Metal as can be seen from the full stress vs. strain  
67 curve in Figure 2. A total of 20 load-unload cycles were carried out. The macroscopic  
68 strain was recorded using a 10 mm contact extensometer.

69 The Debye-Scherrer diffraction rings formed by the monochromated incident X-ray  
70 beam (0.5×0.5 mm, 80 keV ( $\lambda=0.15498 \text{ \AA}$ )) were imaged using a Thales Pixium RF4343  
71 2880×2880 pixel 2D area detector positioned 1320.725 mm from the specimen. The im-  
72 ages were acquired using 2 s exposures, while the detector’s write time was a further 0.5 s  
73 per image.

74 The diffraction ring images were processed using the FIT2D [12] analysis software to  
75 obtain the intensity vs.  $2\theta$  (scattering angle) spectra. The data are taken from a 10°  
76 azimuthal bin around 90°, i.e. aligned to the tensile axis. The instrument parameters  
77 necessary for the analysis were determined using a powder standard. The Wavemetrics  
78 IGOR Pro software package was then used to perform fitting of a Gaussian function to  
79 the individual lattice peaks observed in the integrated spectra.

## 80 2.3. *Post-mortem electron microscopy*

81 Screw-threaded fatigue specimens with a round cross section, a gauge diameter of 5 mm  
82 and gauge length of 19 mm were prepared using EDM. In order to help isolate the effects  
83 various deformation related phenomena the specimens were subjected to sub-yield cyclic  
84 loading in both the superelastic regime 15-750 MPa, as well as below the superelastic  
85 transition stress between 15-300 MPa. Furthermore, different numbers of load-unload  
86 cycles were investigated: 1, 2, 20 and 200 cycles at a loading rate of 4 MPa s<sup>-1</sup>. A 100 kN  
87 Instron servo-hydraulic thermo-mechanical fatigue (TMF) frame was used to carry out  
88 the mechanical tests with a contact extensometer to record the macroscopic strain.

89 Subsequent to cyclic testing, the specimens were sectioned perpendicular to the load-  
90 ing axis for electron microscopy. Thicker sections were used to prepare specimens for  
91 electron backscatter diffraction (EBSD) mapping in the Zeiss Auriga field emission gun  
92 scanning electron microscope (FEG SEM) with an Oxford Instruments HKL Nordlys  
93 EBSD detector. Specimen surface preparation involved mechanical grinding using silicon

carbide paper followed by polishing using colloidal silica suspension neutralised to  $\approx$ pH7 using hydrogen peroxide.

Thin slices were used to prepare specimens for transmission electron microscopy (TEM). Spark erosion was used to prepare 3 mm discs, which were then subjected to twin-jet electropolishing using an 8% solution of sulphuric acid in methanol at 18 V and -40 °C. Imaging of the resulting foils was performed using the JEOL JEM 2000FX 200 keV thermionic emission TEM and the FEI Titan 80/300 FEG  $C_s$  aberration corrected TEM/STEM at 300 keV.

### 3. Results

#### 3.1. Macroscopic stress-strain behaviour

Figure 2 shows the stress vs. strain curves recorded during 200 load-unload cycles carried out on the TMF load frame. The first observation is the apparent accumulation of permanent plastic strain after every cycle, visible as gradual drift of the stress strain hysteresis greater residual strains. After 200 cycles, a total of approximately 0.2% strain had been accumulated by the specimen.

It can also be seen from the graph that the shape of the macroscopic behaviour changes progressively with every load cycle. For this, it is sufficient to compare the first and last load cycles. These have been highlighted by black dashed lines and are on the left and right respectively. It is clearly evident that the shapes of the two loops are quite different. There are three key observations that can be made:

The first loop confines a much larger area than the last. This implies that the material dissipates significantly more energy per unit volume during the first cycle. It is also worth noting that the overall shape of the first loop is different to those of all subsequent loops. It has a much broader shape when under high stresses. All subsequent loops are approximately three times narrower at their widest point and become progressively closer in shape to a classical hysteresis loop. This suggests that significant changes occur in the material during the first load cycle that alter its ability to accommodate strain during subsequent cycling.

The threshold stress for the superelastic transition is substantially reduced after 200 cycles. In the first loading curve the superelastic transition occurs at approximately 500 MPa. For comparison, this transition occurs at  $\approx$ 200 MPa in the final loading curve. This is a dramatic reduction which is evidence of permanent changes in the alloy that make the onset of superelastic behaviour more favourable when the load is reapplied.

Lastly, there is an apparent reduction in the Young's modulus of the specimen. The gradient of the elastic section of the loading curve drops from  $\approx$ 65 GPa in the first loading curve to  $\approx$ 55 GPa in the 200<sup>th</sup> one.

All of these observations raise important questions about the extent of reversibility of the  $\beta$  to  $\alpha''$  martensitic transformation in Gum Metal. The alloy appears to accumulate permanent mechanical damage during load cycling within the limits of the superelastic regime. To better explain this behaviour and identify its mechanisms one must examine what happens in the material at the microscopic scale, which is described in the following two sections.



137 Figure 3 shows the evolution of the (Intensity *vs.*  $2\theta$ ) diffraction spectrum during tensile  
 138 loading of Gum Metal in the first cycle. As the applied tensile stress is increased past the  
 139 superelastic transition from 15 to 700 MPa, Figure 3(a), we can observe appearance and  
 140 gradual rise in prominence of two distinct diffraction peaks. These peaks correspond to  
 141 the  $\{110\}$  and  $\{132\}$   $\alpha''$  reflections respectively. Thus, our experiments show the same *bcc*  
 142 to orthorhombic diffusionless phase transformation that has been described by Talling et  
 143 al. [3,13].

144 Upon removal of the applied stress, Figure 3(b), the diffraction peaks attributed to the  
 145  $\alpha''$  martensite subsided considerably. This was always found to be the case, irrespective of  
 146 the number of load cycles that the specimen was subjected to. Therefore, any  $\alpha''$  phase  
 147 that may be retained after removal of the load must occupy an insignificant volume  
 148 fraction and therefore is unlikely to be the source of the observed damage accumulation  
 149 in the material. Figure 3 (c), shows the evolution of the fitted area of the  $\{132\}$   $\alpha''$  peak  
 150 during loading and unloading in the first cycle. We observe that the evolution of the  
 151 peak area also exhibits hysteresis and that the final peak area after unloading is smaller  
 152 (i.e. near zero) than that prior to loading. This indicates the  $\alpha''$  that existed within the  
 153 diffracting before the application of stress has reverted back to  $\beta$  on completion of the  
 154 first cycle. Nevertheless, the superelastic transformation itself must play a significant  
 155 role. In order to better understand the observed phenomena, we now turn to examine  
 156 the changes that take place in the matrix phase,  $\beta$ .

157 Taking into account the texture resulting from extrusion, the  $\{110\}$ ,  $\{211\}$  and  $\{220\}$   
 158 reflections were analysed since they all have a component along the loading axis. They  
 159 are persistent, considerably more intense than the  $\alpha''$  peaks and allow for comparatively  
 160 straightforward and reliable fitting. Figure 4 shows the evolution of the peak position for  
 161 these reflections for selected load-unload cycles. The peak positions also exhibit hysteretic  
 162 behaviour and show similar changes to those observed in the macroscopic stress *vs.*  
 163 strain curve in Figure 2. Here one can see the same drastic change in the shape of the  
 164 curve from cycle 1 to cycle 2. In particular, there the same change in the width of the  
 165 hysteresis. Figure 5(c) shows how the hysteresis width of the  $\{110\}$  peak is reduced during  
 166 superelastic load cycling. The rate of reduction is comparatively great at the beginning  
 167 and becomes more gradual after approximately 5 cycles. The reduction in the threshold  
 168 stress for the superelastic transformation can also be observed.

169 In addition, the  $\{211\}$  peak shows peculiar behaviour. In the case of the first cycle,  
 170 an apparently compressive strain is permanently imparted to the system after loading  
 171 and unloading. The overall shape of the stress *vs.* strain loop is similar to the first  
 172 cycles for  $\{110\}$  and  $\{220\}$ , but it is reflected in the vertical axis and rotated  $90^\circ$  about  
 173 the origin. While we observe that none of the load-unload cycles for the three peaks  
 174 formed closed loops, the first cycle of the the  $\{211\}$  peak shows very clearly the most  
 175 noticeable difference between the initial and final strain values. This is yet more evidence  
 176 of permanent changes in the material. Closure of this substantial gap would require a  
 177 compressive stress. Interestingly, during subsequent load-unload cycles the behaviour is  
 178 similar to that exhibited by the  $\{110\}$  and  $\{220\}$  peaks.

179 Lastly, hysteresis drift can be observed in the positions of the  $\{211\}$  and  $\{220\}$  peaks,  
 180 which appear to accumulate compressive and tensile strain respectively. The  $\{110\}$  peak

181 position also exhibits accumulation of tensile strain after twenty load-unload cycles,  
182 though this change is less noticeable than that those of the other two peaks.

183 Other properties of the three diffraction peaks, ( $\{110\}$ ,  $\{211\}$  and  $\{220\}$ ), also change  
184 during load cycling and provide additional evidence of mechanical damage accumulation.  
185 Figure 5(a) shows that the fitted width of the three peaks increases with each subsequent  
186 load-unload cycle. This increase is gradual for the  $\{110\}$  and  $\{220\}$  widths. In comparison,  
187 the behaviour of the  $\{211\}$  is very peculiar, showing quite a rapid increase in width during  
188 the first 5-6 load-unload cycles. After that, the width continues to increase gradually at  
189 a similar rate to the other two.

190 The diffraction elastic constants (DECs) measured using lattice strains also show a  
191 decreasing trend, Figure 5(b). (A DEC is defined by the gradient of the initial microscopic  
192 stress with respect to the measured elastic lattice strain for a given lattice plane or  
193 family of lattice planes. In this study DECs were evaluated between 20 and 200 MPa.)  
194 The  $\{110\}$  and  $\{220\}$  DECs show a large drop after the second cycle. After that, they  
195 decrease linearly at a slower rate. In contrast, the  $\{211\}$  stands out again. The initial  
196 dramatic drop in the DEC is spread over the first 5-6 cycles. This is then followed by a  
197 slight increase until cycle 10, after which the DEC decreases at approximately the same  
198 rate as the  $\{110\}$  and  $\{220\}$ .

199 The results of the X-ray scattering experiment strongly suggest that significant struc-  
200 tural changes (*i.e.* so called mechanical damage) take place in the Gum Metal specimen  
201 during superelastic load cycling which lead to the observed behaviour. The results sug-  
202 gest that the  $\alpha''$  martensite transforms back to  $\beta$  when the sample is unloaded. Thus, the  
203 mechanisms of the damage accumulation must take place at very fine length scales. To  
204 shed some light on this, we performed the following examination of the microstructure  
205 in the extruded material and load-cycled specimens.

### 206 3.3. Electron microscopy

207 The extruded bar was sectioned, polished using colloidal silica suspension, etched using  
208 8 vol.% HF and 15vol.% HNO<sub>3</sub> in water and examined in a visible light microscope.  
209 Sections taken perpendicularly to the extrusion direction showed extensive ‘marbling’  
210 that is characteristic of cold-deformed *bcc* material. This indicates that the microstructure  
211 is not fully recrystallised after extrusion. It also suggests that not all of the plastic  
212 deformation sustained during the extrusion process has been recovered.

213 Figure 6 shows the results of the EBSD analysis performed on the un-cycled Gum Metal  
214 bar normal to the extrusion direction. The analysis shows that the material exhibits a  
215 strong texture, with the  $\langle 110 \rangle$  crystallographic axes of the grains aligned to the extrusion  
216 direction, Figure 6(b) and (c). More interestingly however, the composite band contrast  
217 and Euler angle map in Figure 6(a) shows the nature of the ‘marbling’ effect. The highly  
218 textured grains appear to form clusters in which their crystallographic misorientation  
219 relative to one another is small. Indeed, TEM shows that many grains are often separated  
220 by low-angle twist or tilt boundaries. A characteristic example boundary can be seen in  
221 the top right hand corner of Figure 7(a). Thus, crystallographic defects may propagate  
222 more easily between the grains within these domains.

223 Bright field TEM overviews of the dislocation content in the extruded and 200 cycle  
224 specimens are presented in Figure 7. From Figure 7(a) one can see that the extruded ma-

225 terial already contains a population of dislocations. These are observed either as isolated  
226 segments or as networks. No significant changes to the arrangement and distribution of  
227 dislocations were observed in the specimen that was subjected to only one load-unload  
228 cycle.

229 However, after 200 cycles, we observe not only an apparent increase in the number  
230 density of dislocations, but also the formation of distinct slip bands, Figures 7(b) and  
231 (c). These bands are not observed in the un-cycled material, neither are they present  
232 after the first load cycle. This indicates that the formation and growth of the slip bands  
233 is a gradual process that leads to the accumulation of plastic strain during load cycling.  
234 Thus, it is the most likely explanation for the hysteresis drift observed in Figure 2.

235 The gradual broadening of the diffraction peaks in Figure 5(a) is also consistent with  
236 this observation. The crystal lattice is distorted by a dislocation core, whereby it is either  
237 under compression or tension. Thus, accumulation of plastic strain can be observed as  
238 the broadening of the diffraction peaks in X-ray and neutron scattering experiments  
239 [14]. However, while all three of the diffraction peaks Figure 5(a) exhibit broadening,  
240 the most dramatic change takes place in the width of the  $\{211\}$  peak. Furthermore,  
241 this change takes place over the first few cycles. This implies that either there is another  
242 deformation related phenomenon contributing to the broadening, or that the number  
243 density of dislocations causing the broadening increases tremendously during the first  
244 few load-unload cycles.

245 Figure 8 illustrates the effect of superelastic load-cycling on the distribution of the  $\omega$   
246 phase precipitates. (Both dark field images taken using the  $\omega$  satellite spots near the  
247  $\{110\}$  zone axis and the corresponding diffraction patterns are shown.) In Figure 8(a),  
248 we see that the material in the as extruded condition already has a population of fine  
249  $\omega$ . However, it should be noted that this distribution is quite uneven and grains still  
250 exist with hardly any precipitates at all. In other instances, the  $\omega$  phase can be found  
251 concentrated in isolated pockets near grain boundaries. This may be a consequence of the  
252 hot extrusion process, which results in the highly deformed and textured microstructure,  
253 as is evident in Figure 6.

254 Subjecting the Gum Metal to a single load-unload cycle appears to increase the fraction  
255 of the  $\omega$  phase precipitates, as well as their apparent size, Figure 8(b). This is evident  
256 in both the dark field image and the diffraction pattern, where the  $\omega$  satellite spots are  
257 considerably brighter. This observation is consistent with the finding of Jones et al. [8],  
258 who also observed this trend. In contrast with the un-cycled material, the  $\omega$  phase was  
259 also more evenly distributed throughout the TEM specimen. After 200 cycles, we observe  
260 that the amount of the  $\omega$  phase has increased further, Figure 8(c). The precipitates also  
261 appear to have either increased in their average size, or to have formed distinct clusters.

262 The observed formation of  $\omega$  phase during the first load-unload cycle coincides with a  
263 change in the shape of the hysteresis loop that is evident between the first and second  
264 cycles. Thus, it is likely that the superelastic behaviour is affected by the precipitation  
265 of  $\omega$ . Our observations suggest an increase in the  $\omega$  fraction correlates with the gradual  
266 decrease in the threshold stress for the superelastic transition. It is possible that the  
267 presence of  $\omega$  somehow facilitates the martensitic phase transformation responsible for  
268 superelastic behaviour. It should also be noted that the formation of slip bands may also  
269 be contributing to this phenomenon. We therefore propose that a detailed study is carried  
270 out using small angle neutron/X-ray scattering (SANS/SAXS) to assess the dependence  
271 of the  $\omega$  volume fraction and size distribution on superelastic load cycling.

272 Twinning of the *bcc*  $\beta$  phase is also observed in specimens that have been subjected  
273 to 200 load-unload cycles. The twinned structures are of two types: solitary laths and  
274 colonies. Examples of the solitary twins imaged close to the  $\{110\}$  zone axis are shown  
275 in Figure 9(a-d). They have thicknesses ranging from  $\approx 5$  to 50 nm and their ends are  
276 tapered to a point, Figure 9(d). Such morphology is characteristic of deformation twins  
277 [15]. Figure 9(e) shows a pseudo diffraction pattern (frequency domain image) generated  
278 using a fast Fourier transform (FFT) of the high-resolution lattice image in Figure 9(c).  
279 (N.B. Figure 9(b) shows the same twin at lower magnification.) The spot pattern confirms  
280 that the structure is indeed twinned  $\beta$  phase. Figure 9(f) is a schematic of the pattern in  
281 (e), where the red and pink spots correspond to the material within the lath and black  
282 and grey spots to the material that surrounds it. From the lattice images and diffraction  
283 patterns in Figure 9 it is possible to deduce that the interface plane of the twin and the  
284 surrounding material is close to the  $\{112\}$ . It is peculiar that these deformation twins are  
285 only observed in grains that feature slip bands, and are typically found within the slip  
286 bands themselves running parallel to them, as can be seen in Figure 9(a). This suggests  
287 that one type of defect structure may act as the source of the other.

288 Figure 10 shows an example of a twin colony found in a specimen that was subjected to  
289 200 load-unload cycles. Due to the bending of the TEM specimen, the diffraction contrast  
290 bright field image in 10(a) reveals very well the structure of the colony. One can see  
291 smaller twins within larger twinned regions. Figure 10(b) shows, at greater magnification,  
292 the structure of the finer twins in the region marked by the square in Figure 10(a). The  
293 six twins visible in the image have been numbered from left to right. The region imaged  
294 in Figure 10(b) is aligned to a zone axis (visible from the bend contours in Figure 10(a))  
295 phase contrast imaging of the lattice is possible. Figure 10(c) shows the lattice structure  
296 of twin 5 and the interface with the surrounding twins. The banding of the interface  
297 results from the interface planes not being normal to the image plane, causing slight  
298 overlap of the twinned crystal in the image.

299 Figure 10(d) shows the FFT frequency domain images of twinned regions 1-4. The spot  
300 patterns indicate that the viewing direction in Figure 10(c) is parallel to the  $\{012\}$  zone  
301 axis of the *bcc*  $\beta$  phase and that the observed structures are indeed twins. The measured  
302 average values of  $d_{\{002\}}=1.650 \text{ \AA}$  and  $d_{\{112\}}=1.345 \text{ \AA}$  (to 4 significant figures) give the  
303 corresponding values for the lattice constant of  $3.300 \text{ \AA}$  and  $3.295 \text{ \AA}$ . These fit well with  
304 the lattice parameter measured using synchrotron X-ray diffraction,  $3.2907 \text{ \AA}$ . The values  
305 measured from the electron image may be larger due to heating imparted on the sample  
306 by the electron beam. Diffuse streaking and interference spots can be distinguished in  
307 the frequency domain images, particularly well for twin 3. These are likely to correspond  
308 to the abundant  $\omega$  phase. The particular morphology of the twins suggests that they may  
309 have originated *via* the reverse transformation of the twinned  $\alpha''$  phase back to the *bcc*  
310  $\beta$  phase upon unloading.

#### 311 4. Discussion

312 The results of our study show that load cycling of Gum Metal in the superelastic regime  
313 induces permanent microstructural changes. Furthermore, the extent and nature of these  
314 changes depends on the number of load cycles sustained by the material. In order to better  
315 understand the causes of the observed phenomena, we now consider the nature of the

316 superelastic transformation in Gum Metal. For this, we can employ the phenomenological  
 317 theory of martensitic transformation (PTMT) as outlined by Lieberman, Wechsler and  
 318 Read [16,17] and Mackenzie and Bowles [18–21] to model the cubic to orthorhombic  
 319 transformation of  $\beta$  to  $\alpha''$ .

320 The theory allows the prediction of the interface plane, orientation relationships and  
 321 macroscopic distortions for the transformation using only the lattice parameters of the  
 322 austenite and martensite phases as an input. It shows that an interface plane with zero  
 323 distortion (i.e. an invariant plane) minimises the strain energy associated with the trans-  
 324 formation. This is achieved through the twinning of the martensite phase in such a way  
 325 where the relative amounts of the two twin variants,  $x_1$  and  $x_2$  where  $x_1 = 1 - x_2$ , satisfy  
 326 this condition.

327 In our calculation we used the following lattice parameters which were measured  
 328 experimentally during the in-situ synchrotron experiment:  $a_\beta=3.347\text{\AA}$ ,  $a_{\alpha''}=3.225\text{\AA}$ ,  
 329  $b_{\alpha''}=4.763\text{\AA}$ ,  $c_{\alpha''}=4.636\text{\AA}$ . For comparison, the values reported by Talling et al. [3] were  
 330 also subjected to the analysis ( $a_\beta=3.347\text{\AA}$ ,  $a_{\alpha''}=3.250\text{\AA}$ ,  $b_{\alpha''}=4.853\text{\AA}$ ,  $c_{\alpha''}=4.740\text{\AA}$ ).  
 331 All results are reported relative to the cubic crystal coordinate system of the parent  $\beta$   
 332 phase. It should also be noted that left-handed coordinate axes were used, following the  
 333 methodology of the original manuscript by Lieberman et al. [16].

334 According to their approach the total distortion  $\mathbf{E}$  caused by the transformation  
 335 is given by the following expression:

$$\mathbf{E} = (1 - x_2)\mathbf{\Phi}_1\mathbf{T}_1 + x_2\mathbf{\Phi}_2\mathbf{T}_2 \quad (1)$$

336 The matrices  $\mathbf{T}_1$  and  $\mathbf{T}_2$  describe the Bain [22,17] distortion for each martensite variant.

337 In the cubic (austenite) reference frame these these were defined as

$$\mathbf{T}_1 = \begin{pmatrix} \eta_1 & \eta_2 & 0 \\ \eta_2 & \eta_1 & 0 \\ 0 & 0 & \eta_3 \end{pmatrix} \quad \text{and} \quad \mathbf{T}_2 = \begin{pmatrix} \eta_1 & 0 & \eta_2 \\ 0 & \eta_3 & 0 \\ \eta_2 & 0 & \eta_1 \end{pmatrix} \quad (2)$$

338 where  $\eta_1 = \sqrt{2}(b_{\alpha''}+c_{\alpha''})/4a_\beta$ ,  $\eta_2 = \sqrt{2}(-b_{\alpha''}+c_{\alpha''})/4a_\beta$  and  $\eta_3 = a_{\alpha''}/a_\beta$ . The rotations

339 necessary to attain a zero distortion plane are given by the matrices  $\mathbf{\Phi}_1$  and  $\mathbf{\Phi}_2$ . The  
 340 PTMT first calculates the relative rotation between  $\mathbf{\Phi}_1$  and  $\mathbf{\Phi}_2$ . This allows the relative  
 341 amounts of the twin variants,  $x_1$  and  $x_2$ , that are necessary to attain an invariant plane  
 342 to be determined along with the principal distortion matrix,  $\mathbf{F}_d$ , where:

$$\mathbf{F}_d = \begin{pmatrix} \lambda_1 & 0 & 0 \\ 0 & \lambda_2 & 0 \\ 0 & 0 & \lambda_3 \end{pmatrix} \quad (3)$$

343 To satisfy the invariant plane condition, one of the principal distortions,  $\lambda_i$ , must be unity

344 when the correct proportions of the twin variants,  $x_1$  and  $x_2$ , are formed. This condition  
 345 allows one to calculate the solution using linear algebra. This in turn allows the total  
 346 distortion,  $\mathbf{E}$ , to be determined and with it the critical parameters for the transformation

347 including orientation relationship between the austenite and martensite phases are also  
 348 found.

349 Table 1 lists these key properties of the transformation where  $\mathbf{n}$  is the normal to the  
 350 invariant interface plane;  $\mathbf{s}$ ,  $m$  and  $\theta$  are the direction, magnitude and angle of shear  
 351 respectively; while  $\mathbf{t}$  is the twin plane between the two martensite variants. The rotation  
 352 matrices  $\Theta$  and  $\Omega$  transform the cubic planes and directions to the orthorhombic axis  
 353 systems of the martensite variants 1 and 2 respectively. Their components evaluated for  
 354 the lattice parameters measured in this study are shown below and the corresponding  
 355 orientation relationships are given in Table 2.

$$\Theta = \begin{pmatrix} 0.7190 & -0.7039 & 0.0108 \\ 0.6851 & 0.6994 & -0.0255 \\ 0.0102 & 0.0252 & 0.9632 \end{pmatrix}_{\beta \rightarrow \alpha'_1} \quad (4a)$$

$$\Omega = \begin{pmatrix} 0.7136 & -0.0414 & -0.7083 \\ 0.0025 & 0.9620 & -0.0538 \\ 0.6906 & 0.0370 & 0.6936 \end{pmatrix}_{\beta \rightarrow \alpha'_2} \quad (4b)$$

356 Below are the matrices evaluated using lattice parameters measured by Talling et al.  
 357 and the orientation relationships are shown presented in Table 3.

$$\Theta = \begin{pmatrix} 0.7452 & -0.7028 & -0.0438 \\ 0.6877 & 0.7273 & 0.0309 \\ 0.0095 & -0.0503 & 0.9697 \end{pmatrix}_{\beta \rightarrow \alpha'_1} \quad (5a)$$

$$\Omega = \begin{pmatrix} 0.7268 & 0.0192 & -0.7229 \\ -0.0165 & 0.9708 & 0.0092 \\ 0.7061 & 0.0052 & 0.7101 \end{pmatrix}_{\beta \rightarrow \alpha'_2} \quad (5b)$$

358 One can see from these data that the interface and twin planes,  $\mathbf{n}$  and  $\mathbf{t}$  respectively,  
 359 are irrational for both sets of lattice parameters. The implication of this is that these  
 360 interfaces are likely to be semi coherent and feature a stepped geometry that is stabilised  
 361 by the presence of dislocations. This hypothesis is consistent with the experimental evi-  
 362 dence presented in our study since the superelastic transformation results in the creation  
 363 of new interfaces feature lattice defects that lead to an irreversible accumulation of strain.  
 364 That said, the planarity and coherence of these interfaces is difficult to assess: HR TEM  
 365 is sensitive to specimen bending (which is prevalent in foils prepared from highly de-  
 366 formed Gum Metal) and the averaging effect associated with imaging columns of atoms  
 367 also plays a part. Furthermore, no  $\alpha''$  martensite phase is retained in our specimens that  
 368 would permit a direct evaluation.

369 The differences between the the results for the two sets of lattice parameters are also  
 370 of interest. The lattice parameters measured here require two principal distortions that

371 are both smaller than unity, which implies that both are contractions. When using the  
372 parameters of Talling et al., one of the distortions is greater than unity and one is smaller,  
373 with the implication that one is an expansion and the other is a contraction. The over-  
374 all magnitude of shear is also greater for this study. Lastly there is difference in the  
375 relative amounts of the two twin variants. These discrepancies may be a result of differ-  
376 ent techniques used to measure the lattice parameters (Synchrotron XRD vs. electron  
377 diffraction). However, the parameters reported by Talling et al. are actually average  
378 values for alloys with different compositions: Ti-36.9Nb-2.0Ta-3.0Zr-0.30O and Ti-  
379 35.0Nb-2.1Ta-3.1Zr-0.30O wt.%. The Gum Metal used in this study has a lower oxygen  
380 content (0.26 wt.%). This may contribute to the difference in observed lattice param-  
381 eters and the PTMT calculation results, since oxygen concentration is known to have  
382 a strong effect on the martensitic transformation and  $\omega$  phase formation in  $\beta$  titanium  
383 alloys [13,10].

384 The mathematical transformation theory seems to provide a possible explanation for  
385 the formation for the increased dislocation density observed as slip bands in Figure 7.  
386 The glide planes of the dislocation segments making up the slip bands are close to the  
387  $\{112\}$  habit planes of the deformation twins. The interface plane normals,  $\mathbf{n}$ , calculated  
388 using PTMT are irrational. Their normals have a misorientation from  $(1\bar{2}1)_\beta$  of  $\approx 10.0^\circ$   
389 and  $8.0^\circ$  respectively for the two sets of lattice parameters. It is possible that the nec-  
390 essary stepped geometry which is required for the high index irrational interface planes  
391 is accommodated by  $\frac{a}{2}\langle 111\rangle\{112\}$  dislocations. Thus the observed slip bands may be  
392 formed at or within the vicinity of the  $\beta/\alpha''$  interfaces as the material is subjected to  
393 superelastic load cycling. When the load is reapplied during each cycle, the remnant def-  
394 ects may favour the subsequent reformation of the interfaces close to their locations in  
395 the previous cycle. The application of the load is also likely to propagate the generated  
396 dislocations, further contributing to the increase in their number density over time.

397 This in turn sheds light on the origin of the deformation twins in close proximity or  
398 within the slip bands, as shown in Figure 9. The current understanding is that deforma-  
399 tion twins are likely to nucleate and grow via defect assisted mechanisms [15,23]. We  
400 consider that the homogeneous nucleation of twinning dislocations is unlikely. The glide  
401 planes of the dislocation segments making up the slip bands are close to the  $\{112\}$  habit  
402 planes of the deformation twins. This observation is in line with “slip band conversion”  
403 model put forward for b.c.c. metals by Mahajan [24], based on the theories of coupling  
404 between  $\frac{a}{2}\langle 111\rangle\{112\}$  screw dislocation slip and twin nucleation [25–27].

405 The observations discussed thus far suggest that upon removal of the tensile load the  $\alpha''$   
406 phase generally de-twins and reverts back to the  $\beta$  crystal structure. In contrast, Figure  
407 10 shows twinning of a different nature in the  $\beta$  phase. The twin plane is also  $\{112\}$ , so  
408 the observed microstructure is unlikely to have formed via the reverse transformation of  
409 the  $\alpha''$  twins which have a twin plane that is close to  $\{110\}_\beta$ . This leaves two possible  
410 routes for the formation of the twinned  $\beta$  microstructure. In the first, the microstructure  
411 was formed directly via the twinning of the b.c.c. phase. Alternatively, if under load the  
412 preceding structure was comprised of alternating layers of  $\beta$  and  $\alpha''$ , it is possible that  
413 upon removal of the load the the martensite phase underwent a reverse transformation,  
414 but to a twin variant of the original  $\beta$  phase. Thus, the interface  $\beta/\alpha''$  interface planes  
415 would have become twin planes separating two variants of  $\beta$ . This may be possible because  
416 of the relative proximity of the interface plane to  $\{112\}_\beta$ .

417 It is also worth noting that the calculated  $\beta/\alpha''$  interface plane normals have a mis-

418 orientation of  $\approx 9.4^\circ$  and  $12.8^\circ$  (respectively for the two sets of lattice parameters) from  
419  $(\bar{1}\bar{1}\bar{1})_\beta$ , which is the habit plane of the  $\omega$  phase. Thus, its possible that the precipitates  
420 of this phase also help accommodate the irrational interface between the austenite and  
421 martensite phases. Our observations show that load cycling produces more  $\omega$  phase.

422 Thus, both our observations and the classical transformation theory show that defects  
423 are likely to form during the martensitic that gives rise to superelasticity. The generated  
424 defects appear to better accommodate the  $\beta/\alpha''$  interface and thus lower the activation  
425 strain energy required for the martensitic transformation. This is the likely cause of the  
426 of the gradual reduction in the threshold stress for the transformation, as well as the  
427 overall energy dissipated in the hysteresis, observed in Figure 2.

## 428 5. Conclusions

429 In our study we have presented experimental evidence of defect accumulation that  
430 occurs during tensile superelastic load cycling of Gum Metal, which not only imparts  
431 a permanent plastic strain on the material, but also alters its superelastic hysteresis.  
432 The observed defects included dislocations forming distinct slip bands, deformation and  
433 transformation twins were also present and there was a transformation of the  $\beta$  phase to  
434 fine athermal  $\omega$  precipitates.

435 Synchrotron X-ray diffraction has identified peculiar behaviour of the  $\{211\}$  diffraction  
436 peak when binned parallel to the tensile direction, that stood out from that of the  $\{110\}$   
437 and  $\{220\}$  reflections. By carrying out a mathematical analysis of the  $\beta$  to  $\alpha''$  marten-  
438 sitic transformation using classical PTMT we have showed that the austenite/martensite  
439 interface plane is irrational and only  $\approx 8$  to  $10^\circ$  from the  $\{211\}$ . This suggests that  
440 the necessary steps in the interface are accommodated by the  $\frac{a}{2}\langle 111\rangle\langle 112\rangle$  dislocations  
441 forming the slip bands observed in TEM. The slip bands conversion model then explains  
442 the formation of deformation twins on the  $\{211\}$  planes. The  $\beta/\alpha''$  interface plane normal  
443 is also  $\approx 9$  to  $13^\circ$  from the  $\{111\}$ , which suggests that the martensitic transformation  
444 and formation of athermal  $\omega$  phase are also related.

445 The PTMT therefore provides a unified explanation for the origin of the observed  
446 defect structures and the resulting macroscopic behaviour. The gradual accumulation  
447 of defects has significant implications for exploiting the superelastic behaviour of Gum  
448 Metal, particularly in applications such as damping since the strain accumulation and  
449 changes in hysteresis (and thus energy dissipation characteristics) must be carefully taken  
450 into account. This may be overcome by fine tuning the alloy composition to produce an  
451 austenite/martensite interface that is closer to a rational low index plane, the formation  
452 of which would produce a minimal number of dislocations.

## 453 6. Acknowledgements

454 The authors would like to acknowledge financial support provided by the EPSRC  
455 under grant EP/H004882/1 - "Reducing Emissions by Exploiting Field-Induced Marten-  
456 sitic Transformations" (DD) and under the Doctoral Prize Fellowship Scheme (VAV). We  
457 recognise support from the DSTL MAST STC (KMR); the Diamond Light Source for  
458 funding experiment EE6701; Incotest, Hereford, UK for ICP-OES; Prof. Richard Dash-  
459 wood, WMG, University of Warwick, UK for extrusion; Dr. Mahmoud Ardakani, Dept.



460 of Materials, Imperial College London and Dr. Liam Spillane, Gatan UK, Abingdon, UK  
461 for assistance with electron microscopy; Dr. John Webster, Rolls-Royce plc, Derby, UK  
462 for valuable encouragement and discussion of the project.

## 463 References

- 464 [1] T. Saito, T. Furuta, J.-H. Hwang, S. Kuramoto, K. Nishino, N. Suzuki, R. Chen, A. Yamada, K. Ito,  
465 Y. Seno, T. Nonaka, H. Ikehata, N. Nagasako, C. Iwamoto, Y. Ikuhara, T. Sakuma, *Science* 300  
466 (2003) 464–467.
- 467 [2] R. J. Talling, R. J. dashwood, M. Jackson, S. Kuramoto, D. Dye, *Scripta Materialia* 59 (2008)  
468 669–672.
- 469 [3] R. J. Talling, R. J. Dashwood, M. Jackson, D. Dye, *Acta Materialia* 57 (2009) 1188–1198.
- 470 [4] J. W. Morris, Y. Hanlumyuang, M. Sherburne, E. Withey, D. C. Chrzan, S. Kuramoto, Y. Hayashi,  
471 M. Hara, *Acta Materialia* 58 (2010) 3271–3280.
- 472 [5] E. Plancher, C. C. Tasan, S. Sandloebes, D. Raabe, *Scripta Materialia* 68 (2013) 805–808.
- 473 [6] T. Yano, Y. Murakami, D. Shindo, S. Kuramoto, *Acta Materialia* 57 (2009) 628–633.
- 474 [7] T. Yano, Y. Murakami, D. Shindo, Y. Hayasaka, S. Kuramoto, *Scripta Materialia* 63 (2010) 536–539.
- 475 [8] N. J. Jones, R. J. Talling, T. C. Lindley, D. Dye, Failure behaviour and energy adsorption in Gum  
476 metal (Ti-36Nb-2Ta-3Zr-O), in: L. Zhou, H. Chang, Y. Lu, D. Xu (Eds.), *Ti-2011*, Science Press  
477 Beijing, 2012, p. 1169.
- 478 [9] P. Castany, M. Besse, T. Gloriant, *Scripta Materialia* 66 (2012) 371–373.
- 479 [10] M. Besse, P. Castany, T. Gloriant, *Acta Materialia* 59 (2011) 5982–5988.
- 480 [11] E. Eisenbarth, D. Veltens, M. Müller, R. Thull, J. Berne, *Biomaterials* 25 (2004) 5705–5713.
- 481 [12] A. P. Hammersley, S. O. Svensson, A. Thompson, *Nuclear Instruments and Methods in Physics*  
482 *Research A* 346 (1-2) (1994) 312–321.
- 483 [13] E. G. Obbard, Y. L. Hao, R. J. Talling, S. J. Li, Y. W. Zhang, D. Dye, R. Yang, *Acta Materialia* 59  
484 (2011) 112–125.
- 485 [14] N. G. Jones, D. Dye, *Intermetallics* 19 (2011) 1348–1358.
- 486 [15] J. W. Christian, S. Mahajan, *Progress in Materials Science* 39 (1995) 1–157.
- 487 [16] D. S. Lieberman, M. S. Wechsler, T. A. Read, *Journal of Applied Physics* 26 (1955) 473–484.
- 488 [17] M. S. Wechsler, D. S. Lieberman, T. A. Read, *Transactions AIME* 197 (1953) 1503–1515.
- 489 [18] J. S. Bowles, J. K. Mackenzie, *Acta Metallurgica* 2 (1954) 129–137.
- 490 [19] J. K. Mackenzie, J. S. Bowles, *Acta Metallurgica* 2 (1954) 138–147.
- 491 [20] J. S. Bowles, J. K. Mackenzie, *Acta Materialia* 2 (1954) 224–234.
- 492 [21] J. K. Mackenzie, J. S. Bowles, *Acta Metallurgica* 5 (1957) 137–149.
- 493 [22] E. C. Bain, *Transactions AIME* 70 (1924) 25–46.
- 494 [23] S. Mahajan, D. F. Williams, *International Metallurgical Reviews* 18 (1973) 43–58.
- 495 [24] S. Mahajan, *Acta Metallurgica* 23 (1975) 671–684.
- 496 [25] A. W. Sleeswyk, *Philosophical Magazine* 8 (1963) 1467–1486.
- 497 [26] K. Ogawa, *Philosophical Magazine* 11 (1965) 217–233.
- 498 [27] V. Vitek, R. C. Perrin, D. K. Bowen, *Philosophical Magazine* 21 (1970) 1049–1073.
- 499 [28] N. G. Jones, C. M. Ward-Close, P. M. Brown, D. Dye, *Scripta Materialia* 63 (2010) 85–88.

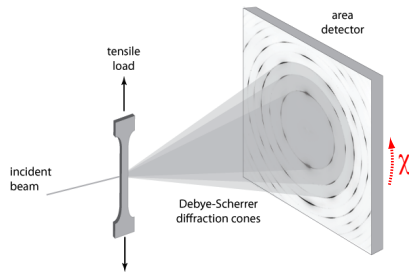


Fig. 1. Schematic representation of the experimental arrangement used to make the in-situ synchrotron measurements. The data are binned over an azimuthal angle,  $\chi$ , to produce intensity vs.  $2\theta$  spectra. Adapted from [28].

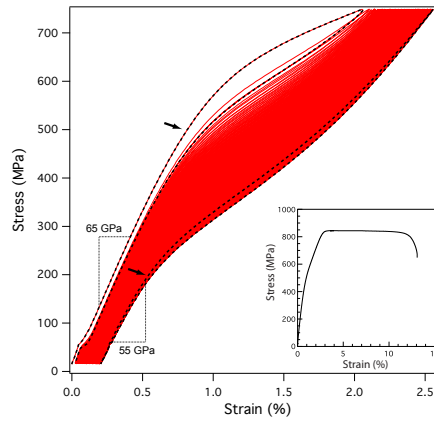


Fig. 2. Evolution of the stress vs. strain hysteresis over 200 load-unload cycles between 15-750 MPa. The loops corresponding to the first (left) and last (right) load cycles are highlighted by the black dashed lines. Arrows show approximate positions of superelastic transition stress upon loading. The full stress vs. strain curve for Gum Metal is shown in the bottom left corner.

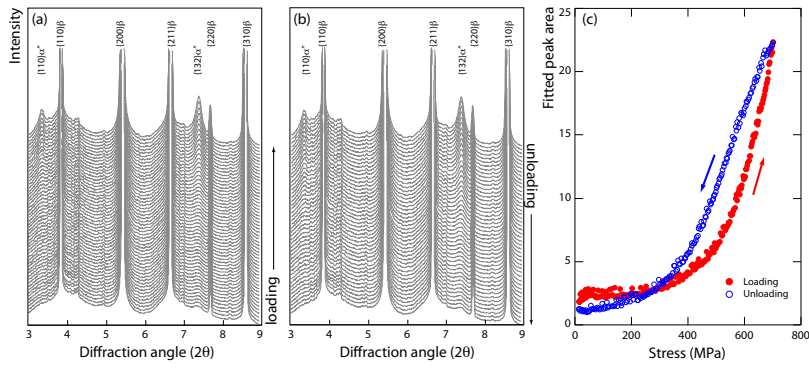


Fig. 3. X-ray scattering spectra for the first load-unload cycle showing the behaviour of  $\alpha''$  scattering peaks amidst those produced by the  $\beta$  phase with increasing (a) and decreasing (b) applied tensile stress (from 15 to 750 MPa). Subfigure (c) shows the evolution of the  $\{132\}_{\alpha''}$  fitted peak area during the first cycle.

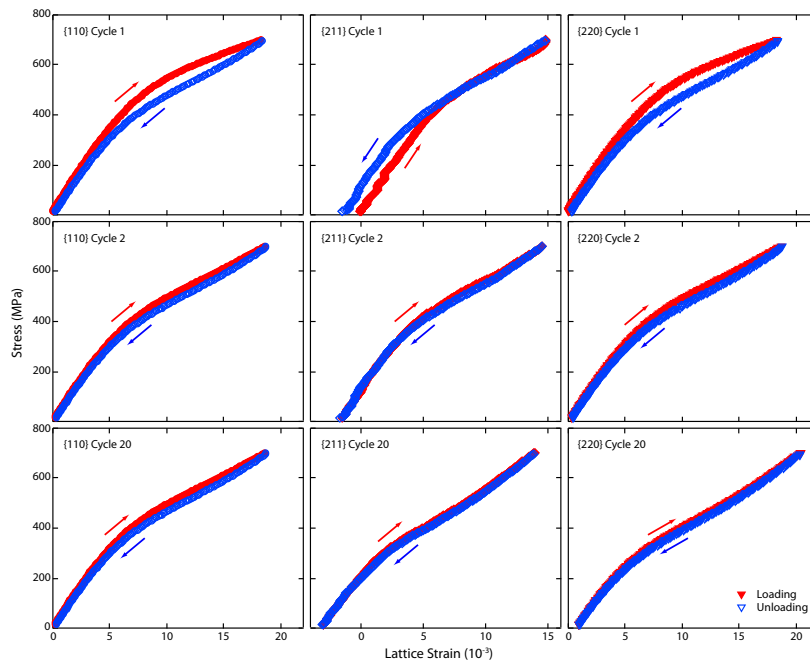


Fig. 4. Evolution of the positions of the  $\beta$  phase  $\{110\}$ ,  $\{211\}$  and  $\{220\}$  X-ray diffraction peaks, all of which have a component along the tensile axis due to the strong texture of the test specimens.

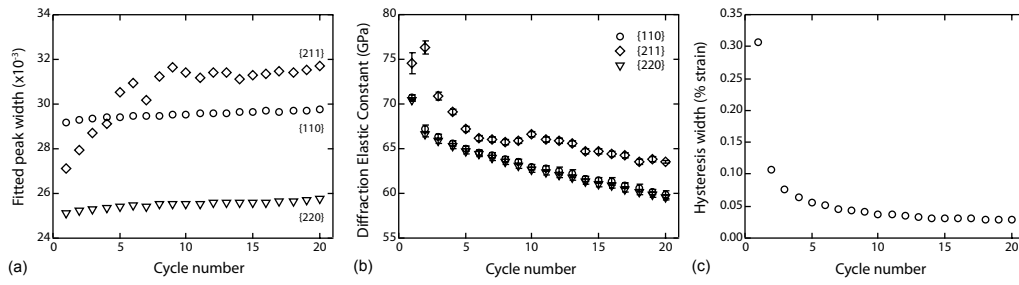


Fig. 5. Changes in the diffraction data of Gum Metal resulting from load cycling in the superelastic regime: (a) broadening of diffraction peaks with components binned parallel to the tensile axis, (b) gradual reduction in the diffraction elastic constants, (c) reduction in the width of the hysteresis loop of the  $\{110\}$  peak taken at the end of each cycle when the sample had been unloaded to 15 MPa and all of the  $\alpha''$  had reverted.

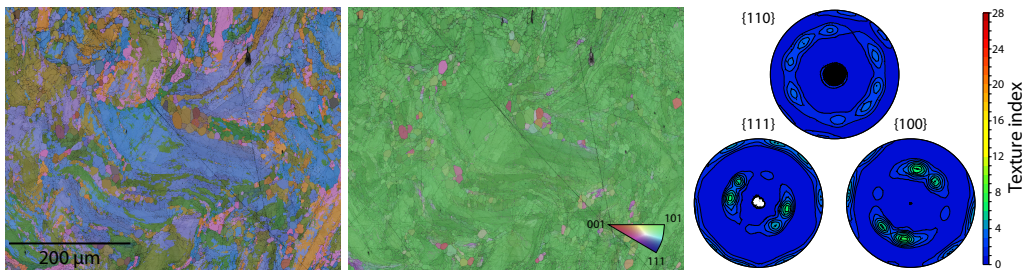


Fig. 6. EBSD analysis of microstructure and texture of the Gum Metal stock normal to the extrusion direction: (a) Euler angle map combined with a band contrast image, (b) inverse pole figure map combined with a band contrast image and (c) pole figures for the  $\{100\}$ ,  $\{110\}$  and  $\{111\}$  directions.

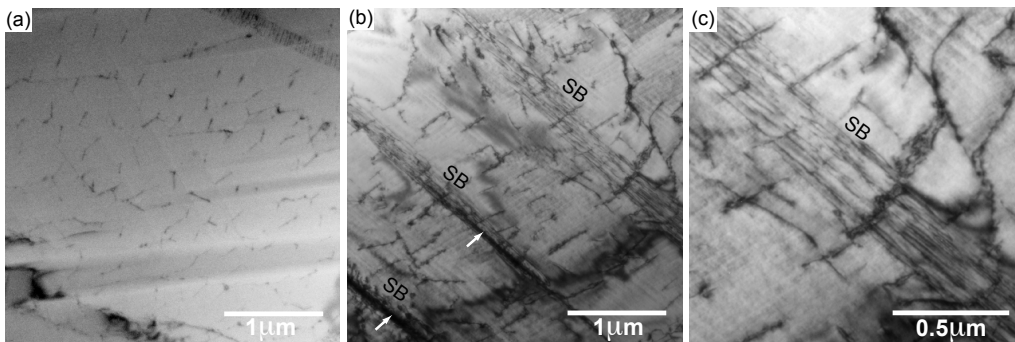


Fig. 7. Diffraction contrast bright-field TEM images showing a comparison of dislocation distributions in the extruded condition (a) and after 200 load-unload cycles (b) and (c). Slip bands have been labelled SB and white arrows point to the locations of deformation twins.

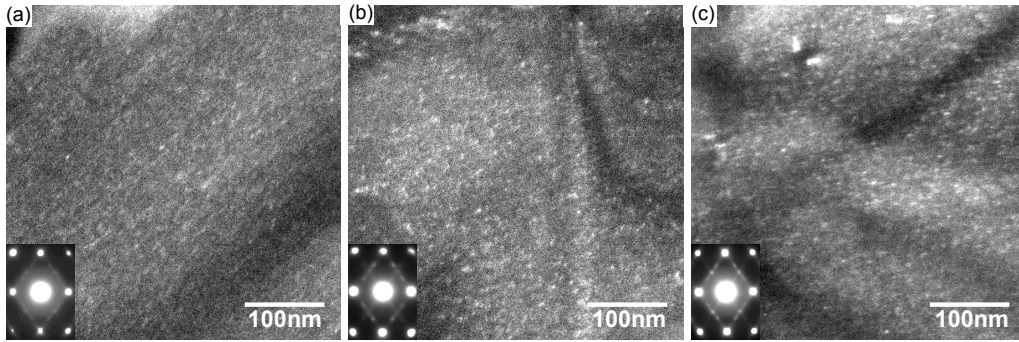


Fig. 8. Dark field TEM micrographs showing that superelastic load cycling increases the amount of the  $\omega$  phase in Gum Metal: (a) as extruded condition, (b) 1 cycle and (c) 200 cycles.

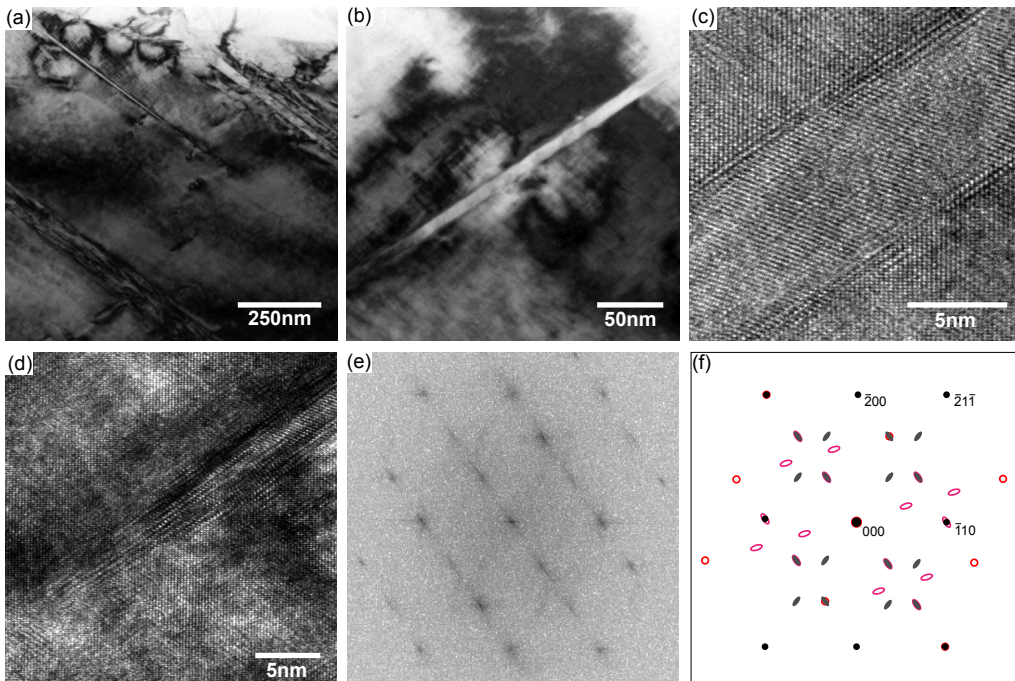


Fig. 9. Diffraction contrast bright field TEM images of fine deformation twins observed after 200 load-unload cycles, (a) and (b). High-resolution phase contrast lattice imaging showing the structure of the twin in the middle (c) and at the tip (d). Frequency domain image (e) obtained using FFT of lattice image (c) and the corresponding schematic denoting showing contributing spot patterns from the twin (red) and the surrounding matrix (black).

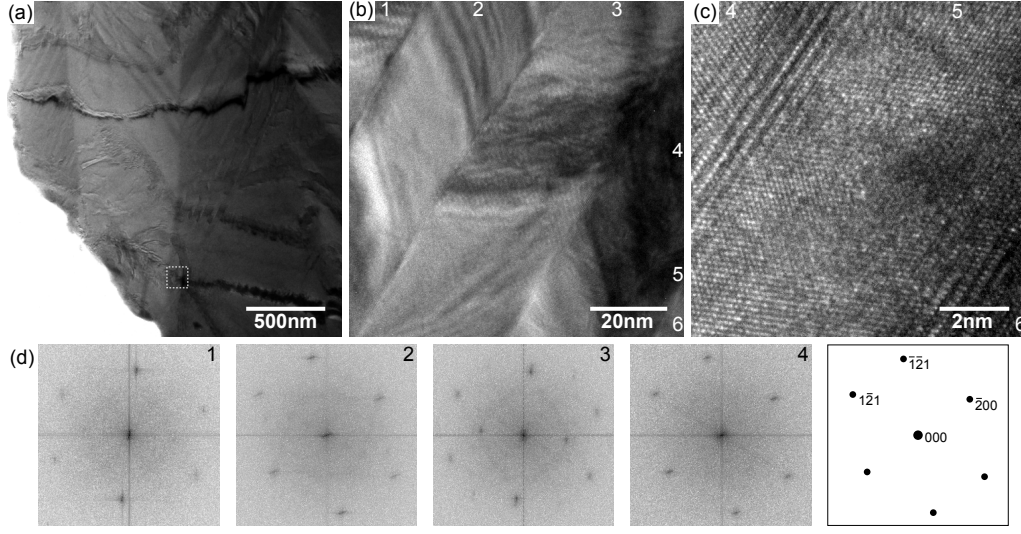


Fig. 10. Diffraction bright field TEM image of a twin colony observed after 200 load-unload cycles, (a) and high-resolution phase-contrast close-up (b) of region marked by the white square in (a). High-resolution phase contrast lattice image (c) of twin 5 in (b). Frequency domain images (d) of obtained using FFT of the lattice in twins 1-4 in (b) and corresponding schematic denoting the Miller indices of the spots in 4.

Table 1

Key properties of the  $\beta \rightarrow \alpha''$  martensitic transformation calculated using PTMT [16]. The top and bottom sets were computed using lattice parameters measured in this study (top) and by Talling et al. [3] (bottom). The parameters, from left to right respectively, are proportions of the  $\alpha''$  twins,  $x_1$  and  $x_2$ , distortion matrix,  $\mathbf{F}_d$ , interface plane normal,  $\mathbf{n}$ , direction of shear,  $\mathbf{s}$ , magnitude of shear,  $m$ , angle of shear,  $\theta$  and  $\alpha'$  twin plane,  $\mathbf{t}$ . All vectors are quoted with respect to the cubic coordinate axes of the  $\beta$  phase.

$x_1 : x_2$	$\mathbf{F}_d$	$\mathbf{n}$	$\mathbf{s}$	$m$	$\theta$	$\mathbf{t}$
74.0 : 26.0	$\begin{pmatrix} 1.000 & 0 & 0 \\ 0 & 0.970 & 0 \\ 0 & 0 & 0.979 \end{pmatrix}$	$\begin{pmatrix} 0.496 \\ -0.708 \\ -0.503 \end{pmatrix}$	$\begin{pmatrix} 0.693 \\ 0.672 \\ -0.263 \end{pmatrix}$	0.050	$1.93^\circ$	$\begin{pmatrix} 0.005 \\ -0.658 \\ 0.714 \end{pmatrix}$
11.5 : 88.5	$\begin{pmatrix} 1.022 & 0 & 0 \\ 0 & 0.976 & 0 \\ 0 & 0 & 1.000 \end{pmatrix}$	$\begin{pmatrix} 0.514 \\ -0.740 \\ -0.443 \end{pmatrix}$	$\begin{pmatrix} 0.593 \\ 0.672 \\ -0.444 \end{pmatrix}$	0.046	$2.66^\circ$	$\begin{pmatrix} 0.019 \\ -0.732 \\ 0.688 \end{pmatrix}$

Table 2

Orientation relationships obtained using lattice parameters measured in this study.

$\beta$ and $\alpha''$ twin 1	$\beta$ and $\alpha''$ twin 2
$(1\bar{1}0)_\beta$ 0.87° from $(100)_{\alpha''_1}$	$(101)_\beta$ 2.37° from $(100)_{\alpha''_2}$
$(10\bar{1})_\beta$ 1.61° from $(010)_{\alpha''_1}$	$(010)_\beta$ 3.20° from $(010)_{\alpha''_2}$
$(001)_\beta$ 1.61° from $(001)_{\alpha''_1}$	$(101)_\beta$ 2.17° from $(001)_{\alpha''_2}$
$[111]_\beta$ 1.71° from $[011]_{\alpha''_1}$	$[111]_\beta$ 2.48° from $[011]_{\alpha''_2}$
$[11\bar{1}]_\beta$ 1.49° from $[01\bar{1}]_{\alpha''_1}$	$[11\bar{1}]_\beta$ 2.61° from $[110]_{\alpha''_2}$
$[\bar{1}11]_\beta$ 1.49° from $[101]_{\alpha''_1}$	$[\bar{1}11]_\beta$ 2.63° from $[0\bar{1}1]_{\alpha''_2}$
$[\bar{1}\bar{1}\bar{1}]_\beta$ 0.73° from $[10\bar{1}]_{\alpha''_1}$	$[\bar{1}\bar{1}\bar{1}]_\beta$ 2.74° from $[\bar{1}\bar{1}0]_{\alpha''_2}$
$[100]_\beta$ 0.86° from $[110]_{\alpha''_1}$	$[100]_\beta$ 0.22° from $[101]_{\alpha''_2}$
$[0\bar{1}0]_\beta$ 1.61° from $[1\bar{1}0]_{\alpha''_1}$	$[00\bar{1}]_\beta$ 3.20° from $[10\bar{1}]_{\alpha''_2}$

Table 3

Orientation relationships obtained using lattice parameters measured in by Talling et al. [3].

$\beta$ and $\alpha''$ twin 1	$\beta$ and $\alpha''$ twin 2
$(1\bar{1}0)_\beta$ 2.96° from $(100)_{\alpha''_1}$	$(101)_\beta$ 1.09° from $(100)_{\alpha''_2}$
$(10\bar{1})_\beta$ 2.39° from $(010)_{\alpha''_1}$	$(010)_\beta$ 1.11° from $(010)_{\alpha''_2}$
$(001)_\beta$ 3.02° from $(001)_{\alpha''_1}$	$(101)_\beta$ 0.34° from $(001)_{\alpha''_2}$
$[111]_\beta$ 1.74° from $[011]_{\alpha''_1}$	$[111]_\beta$ 0.81° from $[011]_{\alpha''_2}$
$[11\bar{1}]_\beta$ 3.26° from $[01\bar{1}]_{\alpha''_1}$	$[11\bar{1}]_\beta$ 1.07° from $[110]_{\alpha''_2}$
$[\bar{1}11]_\beta$ 2.49° from $[101]_{\alpha''_1}$	$[\bar{1}11]_\beta$ 0.58° from $[0\bar{1}1]_{\alpha''_2}$
$[\bar{1}\bar{1}\bar{1}]_\beta$ 3.40° from $[10\bar{1}]_{\alpha''_1}$	$[\bar{1}\bar{1}\bar{1}]_\beta$ 1.12° from $[\bar{1}\bar{1}0]_{\alpha''_2}$
$[100]_\beta$ 1.72° from $[110]_{\alpha''_1}$	$[100]_\beta$ 0.98° from $[101]_{\alpha''_2}$
$[0\bar{1}0]_\beta$ 3.40° from $[1\bar{1}0]_{\alpha''_1}$	$[00\bar{1}]_\beta$ 0.57° from $[10\bar{1}]_{\alpha''_2}$